




Cite this: DOI: 10.1039/d3gc04537d

Engineering built-in electric fields in oxygen-deficient MnO-CeO₂@Cs catalysts: enhanced performance and kinetics for the oxygen reduction reaction in aqueous/flexible zinc–air batteries†

Lixia Wang,^a Xinran Hu,^a Huatong Li,^a Zhiyang Huang,^a Jia Huang,^a Tayirjan Taylor Isimjan^{*b} and Xiulin Yang  ^{*a}

Deliberate engineering of built-in electric fields (BEFs) can facilitate electron transfer and promote asymmetrical charge distribution, thereby regulating the adsorption/desorption of reaction intermediates. Herein, an oxygen-deficiency-rich MnO-CeO₂ is synthesized supported on a carbon sphere (MnO-CeO₂@Cs), adeptly crafted with a prominent work function difference ($\Delta\Phi$) and robust BEF, targeting the electrocatalytic oxygen reduction reaction (ORR). Empirical and theoretical results substantiate that the BEF triggers interfacial charge redistribution, fine-tuning the adsorption energy of oxygen intermediates and hastening reaction kinetics. Consequently, the MnO-CeO₂@Cs showcases commendable performance ($E_{1/2} = 0.80$ V and $j_L = 5.5$ mA cm⁻²), outshining its single-component counterparts. Impressively, the MnO-CeO₂@Cs-based zinc–air batteries (ZABs) boast an exemplary power density of 202.7 mW cm⁻² and enduring stability of 297 h. Additionally, the solid-state ZAB commands a peak power density of 67.4 mW cm⁻², underscoring its potential in flexible ZAB applications. This work delineates a strategic avenue to harness interfacial charge redistribution, aiming to enhance the catalytic performance and longevity of energy conversion/storage apparatuses.

Received 21st November 2023,

Accepted 29th December 2023

DOI: 10.1039/d3gc04537d

rsc.li/greenchem

1. Introduction

Achieving zero-emission goals, critical for tackling climate change, demands the introduction of energy storage and conversion technologies.¹ In this regard, various groundbreaking electrocatalytic devices have been crafted to capture intermittent renewable energy sources and reach carbon neutrality.² Notably, zinc–air batteries (ZABs) stand out due to their high theoretical energy density, cost-effectiveness, environmental sustainability, and safety features.^{3,4} However, their utility is hampered by the slow kinetics of the cathodic oxygen reduction reaction (ORR), impacting their energy efficiency and power density.⁵ Historically, platinum-based materials

have been the leading ORR electrocatalysts.^{6,7} Regrettably, their high cost, limited availability, and durability issues hinder their widespread adoption.⁸ Consequently, crafting affordable and efficient ORR electrocatalysts is pivotal for ZAB advancement.⁹

Transition metal oxides are gaining traction as potential oxygen electrocatalysts, with Mn-based oxides drawing attention for their cost-effectiveness and abundant supply.^{10–12} These oxides exhibit excellent capability in facilitating charge transfer and accelerating the decomposition of intermediates.¹³ Moreover, the rare-earth metal oxide CeO₂ is widely employed in various catalytic domains, attributed to its superb catalytic activity and resilience.¹⁴ The reversible redox switch between Ce³⁺ and Ce⁴⁺ in CeO₂ ensures facile electron flow without affecting its structure integrity.¹⁵ To address the limitations of individual components, heterostructure engineering is a powerful tactic, offering more active sites at their interface.¹⁶ Therefore, melding MnO with CeO₂ offers a logical step in ORR catalyst design.

Additionally, a well-orchestrated built-in electric field (BEF), established by merging components with differing Fermi levels, can adeptly modify the electronic configuration of the

^aGuangxi Key Laboratory of Low Carbon Energy Materials, School of Chemistry and Pharmaceutical Sciences, Guangxi Normal University, Guilin 541004, China.

E-mail: xlyang@gxnu.edu.cn

^bSaudi Arabia Basic Industries Corporation (SABIC) at King Abdullah University of Science and Technology (KAUST), Thuwal 23955-6900, Saudi Arabia.

E-mail: isimjant@sabic.com

† Electronic supplementary information (ESI) available. See DOI: <https://doi.org/10.1039/d3gc04537d>

active site and balance the adsorption/desorption kinetics of reactants and intermediates.¹⁷ Significantly, the work function variance between these components creates an inherent driving force and imparts directionality for charge transfer at the interface.¹⁸ Hence, understanding the relation between interfacial BEF and the intermediate adsorption behavior is critical to decoding the core catalytic mechanism of ORR. Introducing vacancies, engineering heterogeneous interfaces, and employing heteroatom doping are powerful strategies for efficiently inducing charge redistribution within electrocatalysts, effectively promoting the formation of a BEF.¹⁹ Moreover, merging heterojunction catalysts with carbon aids enhances electron transfer, invoking mutual benefits from the catalyst-carbon interaction and spatial restrictions of the carbon matrix.²⁰ This can enhance conductivity and catalytic prowess, thus accelerating electron transfer rates and overall catalytic performance.²¹ Besides, introducing oxygen vacancies can serve as active centers in the catalytic reaction, thereby facilitating the reaction kinetics.⁸ For instance, Wang *et al.* adeptly engineered Co_3O_4 through thermal annealing with controllable oxygen vacancies.²² These introduced vacancies triggered the formation of BEF, showcasing remarkable electrochemical performance in Li-ion batteries. Nevertheless, excessive oxygen vacancies can result in morphological changes and structural damage, leading to a reduction in catalytic performance.²³ Thus, balanced oxygen vacancy content in catalysts typically exhibit superior electrocatalytic activity.²⁴

Inspired by these insights, exploring the profound impact of the BEF on ORR catalysts and zinc-air batteries, this study employs DFT calculations to unveil BEF's role in optimizing oxygen intermediate adsorption. Experimental results reveal that the prepared catalyst possessed a pronounced energy difference, prompting electron transfer from MnO to CeO_2 , resulting in a stable BEF at the interface. $\text{MnO-CeO}_2@\text{Cs}$ demonstrate enhanced ORR activity compared to $\text{MnO}@\text{Cs}$ and $\text{CeO}_2@\text{Cs}$, excelling in current density, kinetic density, and half-wave potential. The BEF further improves reaction kinetics, reflected in the smaller Tafel slope. $\text{MnO-CeO}_2@\text{Cs}$ -based zinc-air batteries showcase exceptional performance with accelerated reaction kinetics.

2. Experimental section

2.1. Materials

Glucose ($\text{C}_6\text{H}_{12}\text{O}_6 \cdot 6\text{H}_2\text{O}$), potassium permanganate (KMnO_4 , 99.5%), and absolute ethanol ($\text{C}_2\text{H}_5\text{OH}$, 99.7%) were acquired from xilong chemical Co., Ltd. Dopamine hydrochloride ($(\text{HO})_2\text{C}_6\text{H}_3\text{CH}_2\text{NH}_2 \cdot \text{HCl}$, 98%), polyvinylpyrrolidone (PVP), cerium(III) nitrate hexahydrate ($\text{Ce}(\text{NO}_3)_3 \cdot 6\text{H}_2\text{O}$, 99.95%), zinc acetate ($(\text{CH}_3\text{COO})_2\text{Zn}$, 99%), and commercial Pt/C (20 wt% Pt) were purchased from Shanghai Aladdin Biochemical Technology Co., Ltd. Nafion (5 wt%) was acquired from Alfa Aesar, and potassium hydroxide (KOH, 90%) was obtained from Macklin Biochemical Co., Ltd. All reagents were analytical grade and were used without any further purification.

2.2. Synthesis of carbon spheres (Cs)

Highly dispersed carbon spheres (Cs) were acquired following procedures outlined in previously reported work.²⁵ In a typical synthesis process, 25 μL of 1 M KOH was added to 40 mL of 0.5 M glucose solution under vigorous stirring, until a colorless and transparent solution was obtained. Subsequently, the resulting solution was transferred to a Teflon-lined stainless-steel autoclave at 180 °C for 6 h. The dark brown product was collected by centrifugation, washed multiple times with deionized water and ethanol, and finally dried at 60 °C overnight.

2.3. Synthesis of Mn_3O_4 supported on Cs

50 mg of the above Cs were dispersed in 10 mL of 0.01 M KMnO_4 solution, stirred in air for 30 min to form a uniform purple slurry which was then centrifuged and dried. The resulting powder was oxidation in air at 400 °C for 3 h.

2.4. Synthesis of $\text{MnO-CeO}_2@\text{Cs}$

Firstly, 100 mg Mn_3O_4 was dispersed in 20 mL of deionized water, 0.1 g dopamine hydrochloride and 0.5 g PVP were dispersed in the above solution, followed by adding Tris dropwise to adjust the pH to approximately 8. Subsequently, 0.5 mmol (0.25, 0.50 and 0.75 mmol) $\text{Ce}(\text{NO}_3)_3 \cdot 6\text{H}_2\text{O}$ was included and stirred for 12 h at room temperature. The obtained samples were incubated in N_2 atmosphere for 2 h at 900 °C (800 and 1000 °C).

2.5. Synthesis of $\text{MnO}@\text{Cs}$ and $\text{CeO}_2@\text{Cs}$

The synthetic process for $\text{MnO}@\text{Cs}$ and $\text{CeO}_2@\text{Cs}$ shared similarities with that of $\text{MnO-CeO}_2@\text{Cs}$, albeit with slight variations. $\text{MnO}@\text{Cs}$ was obtained by directly calcining $\text{Mn}_3\text{O}_4@\text{Cs}$, while $\text{CeO}_2@\text{Cs}$ was achieved by directly encapsulating $\text{Ce}(\text{NO}_3)_2 \cdot 6\text{H}_2\text{O}$ with carbon spheres and subsequent calcination at 900 °C.

3. Results and discussion

3.1. Synthesis and structural analysis of catalysts

Fig. 1a depicts the systematic process of crafting $\text{MnO-CeO}_2@\text{Cs}$ nanocomposites. It begins with the formation of glucose carbon spheres through a hydrothermal technique. Subsequently, manganese (Mn) species were introduced into the carbon spheres and subjected to calcination in an oxygen-rich environment, giving rise to Mn_3O_4 nanospheres ($\text{Mn}_3\text{O}_4@\text{Cs}$). Finally, MnO-CeO_2 nanospheres ($\text{MnO-CeO}_2@\text{Cs}$) were obtained by encapsulating dopamine hydrochloride coupled with Ce species, and subjecting to pyrolysis at 900 °C. X-ray powder diffraction (XRD) was employed to characterize the electrocatalyst's crystal structures. The XRD results confirm the effective oxidation of Mn_3O_4 on carbon spheres (Cs), aligning with the JCPDS: 08-0017 reference code, and labelled as $\text{Mn}_3\text{O}_4@\text{C}$ (Fig. S2†).²⁶ The XRD patterns of the comparative samples $\text{MnO}@\text{Cs}$ and $\text{CeO}_2@\text{Cs}$ (Fig. S3†) are consistent with the recognized patterns for MnO

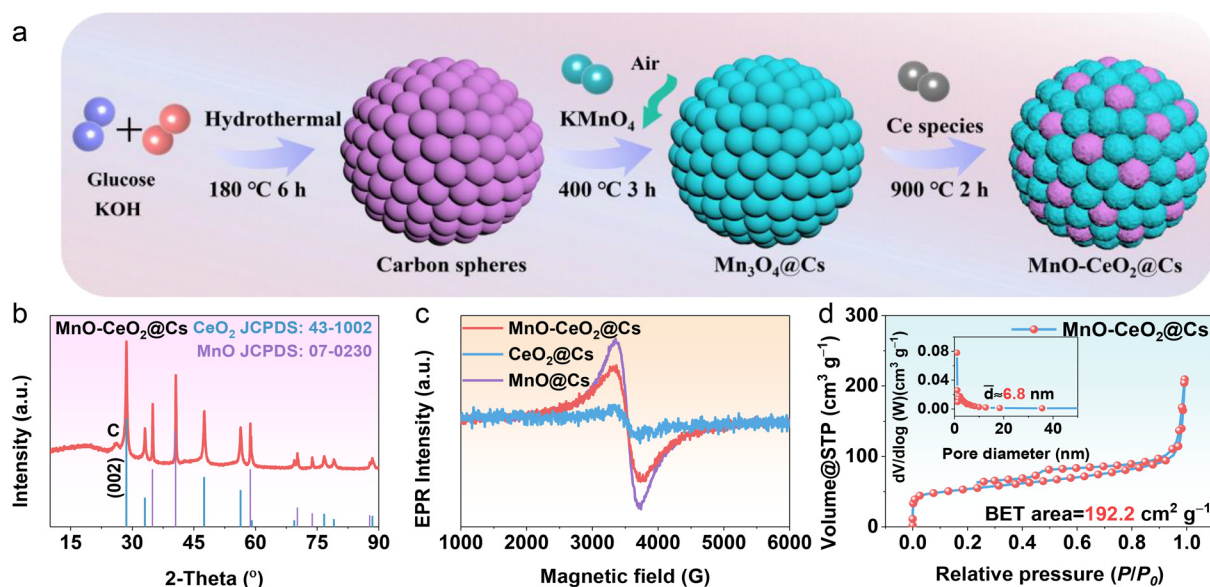


Fig. 1 (a) Schematic illustration of the synthesis process. (b) XRD pattern of MnO-CeO₂@Cs. (c) EPR spectra of as-synthesized samples. (d) N₂ adsorption–desorption isotherm with the inset showing the corresponding pore size distribution of MnO-CeO₂@Cs.

(JCPDS: 07-0230) and CeO₂ (JCPDS: 43-1002), respectively. After coating the Ce species on the Mn₃O₄@Cs precursor, the dominant diffraction peaks align with MnO and CeO₂, with a distinct diffraction peak at 26° attributed to the (002) crystal plane of graphitic carbon (Fig. 1b).²⁷ The D band (1350 cm⁻¹) and G band (1586 cm⁻¹) in the Raman spectra (Fig. S4†) are used to reflect the defects and disorder of sp³ carbon, as well as the graphitization degree of sp² hybrid carbon in the graphite structure, respectively.²⁸ Importantly, graphitized carbon enhances electrical conductivity, and defective carbon provides numerous active sites.²⁹ The I_D/I_G ratios for MnO-CeO₂@Cs, MnO@Cs and CeO₂@Cs were 1.03, 1.12 and 0.97, respectively. This suggests that coupling CeO₂ to MnO@Cs delivers an optimal balance of carbon defects and graphitization, ensuring an optimal number of active sites and commendable electrical conductivity.³⁰ Moreover, fine-tuning the quantity of Ce elements (0.25, 0.50, and 0.75 mmol) and the calcination temperature (800, 900, and 1000 °C), we successfully synthesized MnO-CeO₂@Cs catalysts with varying crystallinity and I_D/I_G values. Remarkably, the catalyst synthesized with 0.50 mmol of Ce species, and pyrolyzed at 900 °C demonstrated the best crystallinity alongside an optimal level of defects and graphitization (Fig. S5 and 6†). These results underscore the substantial impact of the quantity of Ce species and the precise control of calcination temperature on the crystallinity and defect level of MnO-CeO₂@Cs catalysts. Additionally, Fig. 1c displays the electron paramagnetic resonance (EPR) spectra of the samples, with peak intensity positively correlated with the oxygen vacancy content ($g = 2.002$).³¹ Remarkably, MnO@Cs exhibits the highest concentration of oxygen vacancies, attributable to the formation of vacancies during the oxidation with potassium permanganate and calcination processes. Conversely, CeO₂@Cs displays the lowest

concentration of oxygen vacancies, possibly due to the loading of Ce species stabilizing the lattice structure of CeO₂. Interestingly, the coupling CeO₂ in MnO decreases the oxygen vacancy concentration. This phenomenon can be attributed to the interfacial effect between MnO and CeO₂, where the introduction of Ce⁴⁺ replaces some of the Mn²⁺ and occupies the oxygen vacancies.³² Intriguingly, the EPR signals displayed similarity for Ce species added at 0.25 and 0.50 mmol (Fig. S7†). However, increasing the amount to 0.75 mmol led to the strongest EPR signal but suboptimal performance. These findings underscore the significance of fine-tuning the ratio to control the oxygen vacancy concentration, emphasizing the advantage of maintaining a moderate oxygen vacancy concentration for enhancing the electrocatalytic ORR performance. N₂ adsorption–desorption isotherm analysis on the samples revealed reversible type IV curves with a significant hysteresis loop (Fig. 1d and Fig. S8†).³³ Specifically, the specific surface area of MnO-CeO₂@Cs is 192.2 m² g⁻¹, slightly lower than that of MnO@Cs (309.4 m² g⁻¹) and CeO₂@Cs (377.8 m² g⁻¹). This result is attributed to the incorporation of MnO and CeO₂ onto the carbon spheres, leading to the formation of inherent agglomerates during the high temperature calcination process.³⁴ Importantly, all three catalysts showcase a mesoporous structure with a pore size in the range of 5.0–7.7 nm. This mesoporous architecture not only fosters favorable electrolyte-active site interactions but also expedites ion transportation during the ORR process.^{35,36}

The morphology and structural of the catalysts were assessed using scanning electron microscopy (SEM) and transmission electron microscopy (TEM). As shown in Fig. 2a, the synthesized glucose carbon spheres which exhibit the spheres structure with a smooth surface. In Fig. 2b, the SEM images of MnO-CeO₂@Cs depicts a consistent spherical design even

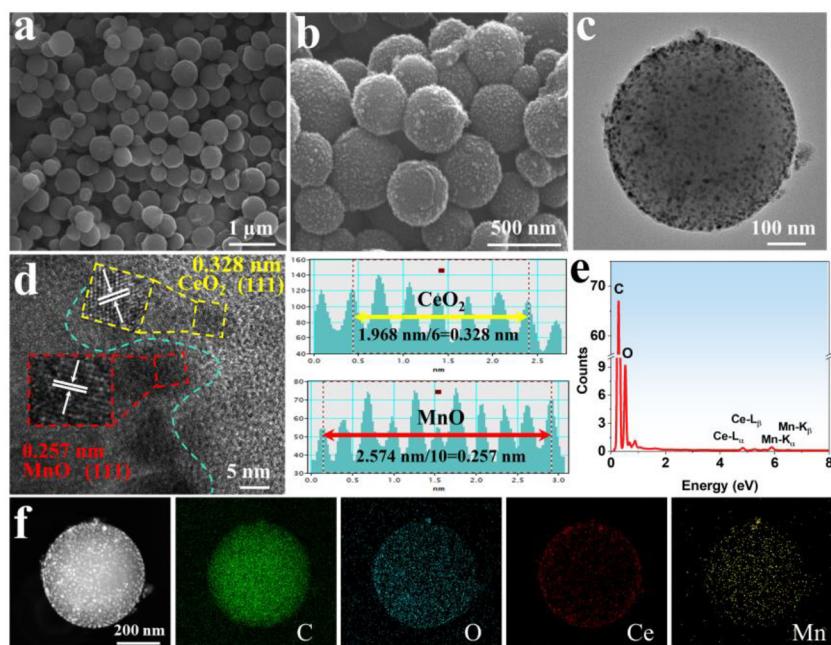


Fig. 2 (a) SEM image of Cs. (b) SEM image, (c) TEM image, (d) HR-TEM image and the corresponding lattice spacing profiles of the dotted line regions, (e) EDS pattern, and (f) HAADF-STEM image and the corresponding elemental mappings of MnO-CeO₂@Cs.

after high-temperature calcination. However, a noticeable alteration is the evolution of its surface to a lychee-like rough and textured appearance. TEM images (Fig. 2c) further illustrated the litchi-like morphology, with the intricate distribution of CeO₂ nanoparticles within the MnO matrix. This embedding process is facilitated during calcination. We have clarified the structural features revealed by the high-resolution TEM (HR-TEM) image, as indicated by the green dashed line in Fig. 2d. This image exposes a well-defined heterostructure between MnO and CeO₂, emphasizing a robust interfacial coupling. The discernible lattice fringes within the heterostructure provide insight into the (111) planes of MnO and CeO₂, with respective spacings of 0.257 and 0.328 nm. Additionally, Fig. 2e offers an energy-dispersive X-ray spectroscopy (EDS) spectrum for MnO-CeO₂@Cs, confirming the presence of C, O, Mn, and Ce elements. Moreover, high-angle annular dark-field STEM (HAADF-STEM) and corresponding elemental mapping disclosed the uniform distribution of C, O, Ce, and Mn across the nanosphere (Fig. 2f). Basic and above, it is plausible that interdiffusion occurs between MnO and CeO₂ rather than the formation of a solid solution. XRD analysis definitively confirms the identical phase composition of MnO-CeO₂@Cs to that of MnO@Cs and CeO₂@Cs. Furthermore, the crystal structure and lattice parameters of MnO-CeO₂@Cs remain consistent with those of the individual material phases. Both SEM and TEM observations reveal an alternating arrangement of the two substances, strongly suggesting interdiffusion between MnO and CeO₂.

Ultraviolet photoemission spectroscopy (UPS) is a pivotal technique for determining the work function of a catalyst. It sheds light on the synergy between a material's electronic pro-

perties and its electrocatalytic activity.³⁷ Essentially, UPS reveals the minimum energy required for electrons to transition from the Fermi level to the vacuum level, suggesting that the lower work function of the catalyst is more conducive to electron transfer.¹⁹ As depicted in Fig. 3a, the band gap of MnO-CeO₂@Cs (4.34 eV) is moderate compared to that of MnO@Cs (4.23 eV) and CeO₂@Cs (4.39 eV). According to the d-band center (ϵ_d) theory, a closer d-band center to the Fermi level (E_f) increases empty antibonding states, enhancing reaction intermediate adsorption.³⁸ The MnO-CeO₂@Cs interfacial structure with a moderate band gap energy, optimized active sites for oxygen intermediates adsorption.³⁹ As visualized in Fig. 3b, the difference creates a gradient, promoting electron movement from higher to lower potential areas. The energy band structure schematic in Fig. 3c illustrates the spontaneous formation of a robust interface BEF from MnO@Cs to CeO₂@Cs.⁴⁰ The interface BEF crucially facilitates charge separation, creating electron-rich regions in CeO₂@Cs and electron-poor regions in MnO@Cs. This enhances the adsorption and dissociation of oxygen intermediates.³⁸ To provide a deeper insight into the catalyst's surface chemistry and elemental composition, X-ray photoelectron spectroscopy (XPS) was employed. The XPS full spectrum (Fig. S9a†) revealed the presence of C, Mn, Ce, and O elements. Diving into the detailed XPS spectra, the high-resolution C 1s spectrum of MnO-CeO₂@Cs presents four separate peaks (Fig. S9b†), corresponding to C=C (284.0 eV), C-C (284.8 eV), C-O (286.0 eV) and C=O bonds (288.8 eV), respectively.⁴¹ In the high-resolution Mn 2p spectrum (Fig. 3d), two pronounced peaks at 641.4 eV (Mn 2p_{3/2}) and 652.5 eV (Mn 2p_{1/2}) can be assigned to Mn²⁺, accompanied by a satellite peak associated with Mn

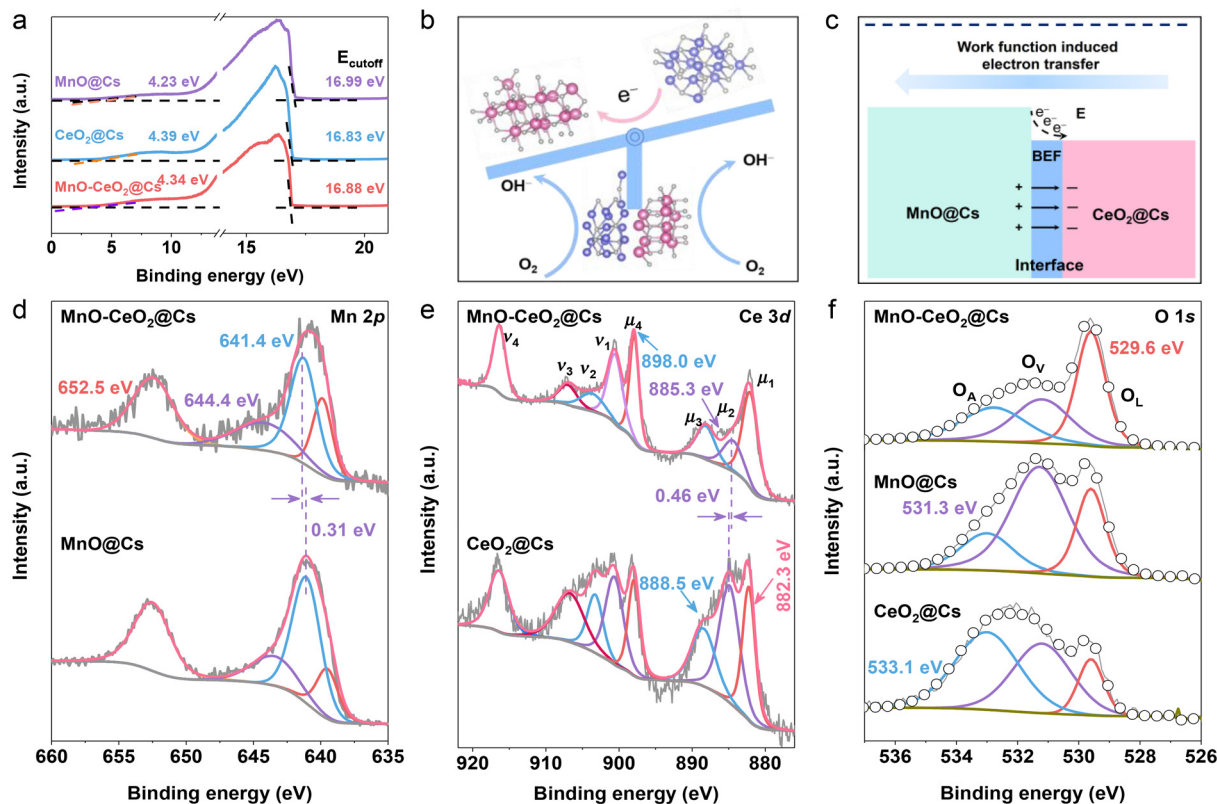


Fig. 3 (a) UPS spectra of MnO@Cs, CeO₂@Cs and MnO-CeO₂@Cs. (b) Proposed ORR process and regulated mechanism of electronic structure in MnO-CeO₂@Cs. (c) Charge transfer process in MnO-CeO₂@Cs. High-resolution XPS spectra of (d) Mn 2p, (e) Ce 3d, and (f) O 1s in MnO-CeO₂@Cs, MnO@Cs and CeO₂@Cs.

$2p_{3/2}$ at 644.4 eV.⁴² The binding energies of Mn²⁺ in MnO-CeO₂@Cs were positively shifted by 0.31 eV compared to MnO@Cs, signifying that the inclusion of CeO₂ leads to a lower valence state of the Mn ion.⁴³ The Ce 3d XPS spectra of MnO-CeO₂@Cs and CeO₂@Cs is presented in Fig. 3e, where μ and ν represent the spin-orbit coupling of Ce 3d_{5/2} and Ce 3d_{3/2}, respectively. Specifically, three sets of peaks at μ_1 (882.3 eV)/ ν_1 (900.6 eV), μ_3 (888.5 eV)/ ν_3 (907.2 eV), and μ_4 (898.0 eV)/ ν_4 (916.4 eV) correspond to three different states of Ce(IV). Meanwhile, a unique peak set at μ_2 (885.3 eV)/ ν_2 (903.9 eV) indicative of Ce(III).⁴⁴ The existence of Ce(III) may be attributed to the reduction of CeO₂, resulting in the release of oxygen and the formation of oxygen vacancies in CeO₂.⁴⁵ Significantly, the μ_2 peak of Ce 3d in MnO-CeO₂@Cs exhibits a negative shift of 0.46 eV compared to CeO₂@Cs, providing further evidence for electron transfer from MnO to CeO₂, echoing the findings from the UPS analysis. As well, the high-resolution O 1s spectra (Fig. 3f) exhibited three main peaks at 529.6 eV, 531.3 and 533.1 eV, which were attributed to lattice oxygen (O_L), oxygen vacancies (O_V) and adsorbed oxygen (O_A), respectively.⁴⁶

3.2. ORR activities in alkaline medium

Considering the profound BEF, the ORR electrocatalytic activity of the various electrocatalysts was appraised in a 0.1 M

KOH solution. Through optimization processes, the prime catalyst was pinpointed and formulated with a Ce species molar count of 0.5 and a calcination temperature of 900 °C, termed MnO-CeO₂@Cs (Fig. S10, 11 and Table S1†). As depicted in Fig. 4a, the cathodic peaks of MnO-CeO₂@Cs is favorably positioned at more electropositive potentials in contrast to MnO@Cs, CeO₂@Cs, and Pt/C, indicating that the constructed BEF conferred its preeminence in ORR activity. Furthermore, MnO-CeO₂@Cs showcases exceptional ORR activity (Fig. 4b), with an onset potential (E_{onset}) and limiting current density (j_L) outclassing its contemporaries and aligning closely with Pt/C, even besting several advanced catalysts (Table S2†). Half-wave potential ($E_{1/2}$) and kinetic current density (J_k) are crucial parameters for assessing ORR performance. As portrayed in Fig. 4c, MnO-CeO₂@Cs demonstrates the highest $E_{1/2}$ value (0.8 V), surpasses both CeO₂@Cs (0.69 V) and MnO@Cs (0.67 V). Moreover, the J_k value of MnO-CeO₂@Cs robustly outperforms its peers, emphasizing its distinguished ORR capabilities. The Tafel slope, indicative of ORR reaction kinetics in electrocatalysts, for MnO-CeO₂@Cs is 37.4 mV dec⁻¹, considerably lower than that of MnO@Cs (81.8 mV dec⁻¹), CeO₂@Cs (62.8 mV dec⁻¹), and Pt/C (65.0 mV dec⁻¹), emphasizing the superior reaction kinetics of MnO-CeO₂@Cs (Fig. 4d).⁴⁷ The electrochemical behavior of MnO-CeO₂@Cs was meticulously scrutinized using ORR polar-

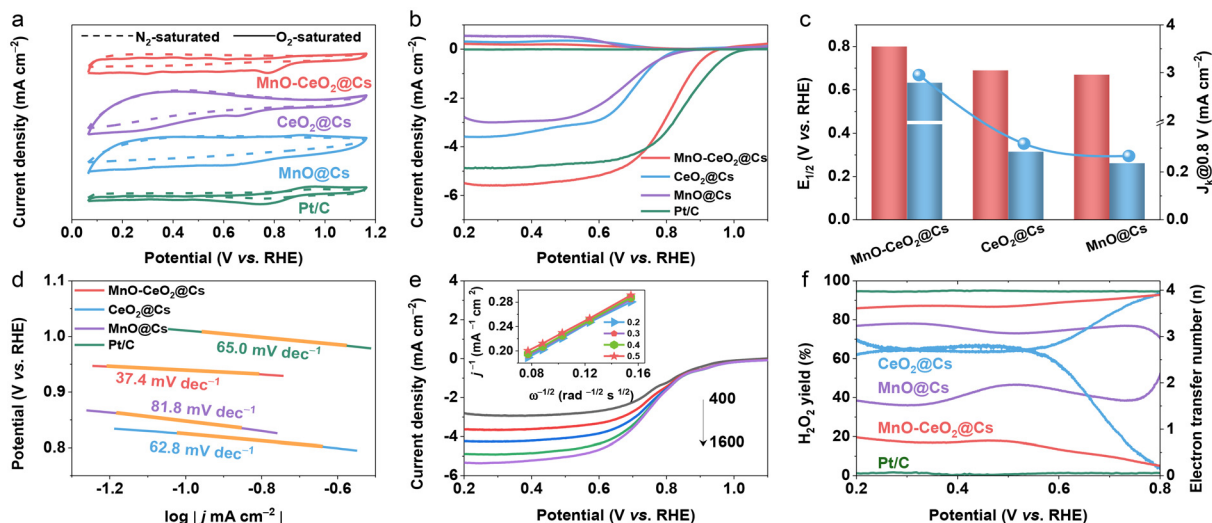


Fig. 4 (a) CV curves in N_2 or O_2 -saturated 0.1 M KOH solutions. (b) LSV polarization curves in O_2 -saturated 0.1 M KOH electrolyte, (c) the corresponding half-wave potential ($E_{1/2}$) and kinetic current density (J_k) at 0.8 V, and (d) Tafel plots of different catalysts. (e) Polarization curves of $\text{MnO-CeO}_2@\text{Cs}$ with various rotating speeds from 400 to 1600 rpm, and the corresponding K–L plots (inset). (f) H_2O_2 yield (%) and electron transfer number (n) from various catalysts.

ization curve tests over various rotation speeds (400–1600 rpm), displayed in Fig. 4e. The corresponding Koutechy–Levich (K–L) plot indicates an electron transfer number (n) nearing 4, proving a predominant four-electron transfer reaction (inset of Fig. 4e).⁴⁸ As illustrated in Fig. 4f, $\text{MnO-CeO}_2@\text{Cs}$ exhibits a low H_2O_2 yield (<20%) and a high electron transfer number (>3.9) in the potential range of 0.2–0.8 V, underscoring its predilection for a direct four-electron ($4e^-$) reduction pathway.⁴⁹

Delving deeper into the electrochemical active surface area (ECSA), CV scans were taken for each catalyst across varied scan rates (Fig. S12[†]). The ECSA of $\text{MnO-CeO}_2@\text{Cs}$ is 201.7 cm^2 , surpassing $\text{CeO}_2@\text{Cs}$ (33.3 cm^2), and showing a slight increase compared to $\text{MnO}@\text{Cs}$ (195.0 cm^2). Despite a small improvement in surface area, $\text{MnO-CeO}_2@\text{Cs}$ performed better than $\text{MnO}@\text{Cs}$ in ORR, showing the importance of the BEF (Fig. S13[†]).⁵⁰ This dominance was further echoed in CV tests using a $\text{K}_3[\text{Fe}(\text{CN})_6]$ solution (Fig. S14[†]). When evaluating methanol tolerance, $\text{MnO-CeO}_2@\text{Cs}$ demonstrated unparalleled resilience against methanol interference, a feat not mirrored by the commercial Pt/C (Fig. S15a[†]).⁵¹ In durability tests spanning 40 000 s (illustrated in Fig. S15b[†]), $\text{MnO-CeO}_2@\text{Cs}$ retained a staggering 99.4% of its initial activity, overshadowing Pt/C. This finding indicates the superior durability of $\text{MnO-CeO}_2@\text{Cs}$, primarily attributed to its porous carbon sphere structure, which facilitates mass charge transport and effectively prevents the aggregation of metal ions during the electrochemical process.⁵² Collectively, the performance of $\text{MnO-CeO}_2@\text{Cs}$ metrics solidify its considerable potential in practical electrocatalytic endeavors.

The $\text{MnO-CeO}_2@\text{Cs}$ catalyst was characterized after stability testing, revealing that it maintained its composition of MnO and CeO_2 , as validated by XRD analysis. SEM images revealed

that the $\text{MnO-CeO}_2@\text{Cs}$ catalyst retained its lyotropic rough appearance, with minimal agglomeration observed (Fig. S16[†]), in agreement with the TEM results. Notably, EDS elemental mapping exhibited a uniform distribution of C, O, Ce, and Mn throughout the entirety of the catalyst, providing compelling evidence for the impressive structural stability displayed by $\text{MnO-CeO}_2@\text{Cs}$.

3.3. Zinc–air batteries test

Given the impressive electrocatalytic performance of $\text{MnO-CeO}_2@\text{Cs}$, we constructed an aqueous ZAB to assess its potential applications in energy storage and conversion devices. In light of the suboptimal OER performance observed in Fig. S17[†], the charge–discharge stability of ZAB was assessed using $\text{MnO-CeO}_2@\text{Cs} + \text{RuO}_2$ (mass ratio = 2 : 1) as the air cathode. Simultaneously, Pt/C + RuO_2 was prepared for comparison. As illustrated in Fig. 5a, the ZAB was equipped with a zinc plate anode, $\text{MnO-CeO}_2@\text{Cs}$ as the cathode, and 6.0 M KOH containing 0.2 M $\text{Zn}(\text{AC})_2$ as the electrolyte. The ZAB built with $\text{MnO-CeO}_2@\text{Cs}$ displayed a commendable open-circuit voltage (OCV) of 1.53 V, outpacing the OCV of the Pt/C (1.41 V) ZAB and other comparative samples (Fig. 5b and Fig. S18a[†]). Notably, the ZAB even powered a “Mn–Ce” LED screen (inset of Fig. 5b). $\text{MnO-CeO}_2@\text{Cs}$ delivered a specific capacity of $802 \text{ mA h g}_{\text{Zn}}^{-1}$, higher than that of Pt/C based ZAB ($699 \text{ mA h g}_{\text{Zn}}^{-1}$), further affirming its exemplary efficiency (Fig. 5c). Encouragingly, the $\text{MnO-CeO}_2@\text{Cs}$ reached a peak power density of 202.7 mW cm^{-2} (Fig. 5d), considerably outperforming the Pt/C (127.6 mW cm^{-2}), $\text{CeO}_2@\text{Cs}$ (159.1 mW cm^{-2}) and $\text{MnO}@\text{Cs}$ -based (99.8 mW cm^{-2}) counterparts (Fig. S18b[†]). When benchmarked against recent advancements in oxide ORR catalysts for ZABs, $\text{MnO-CeO}_2@\text{Cs}$ stands out in both power density and capacity (Fig. 5e and Table S3[†]).

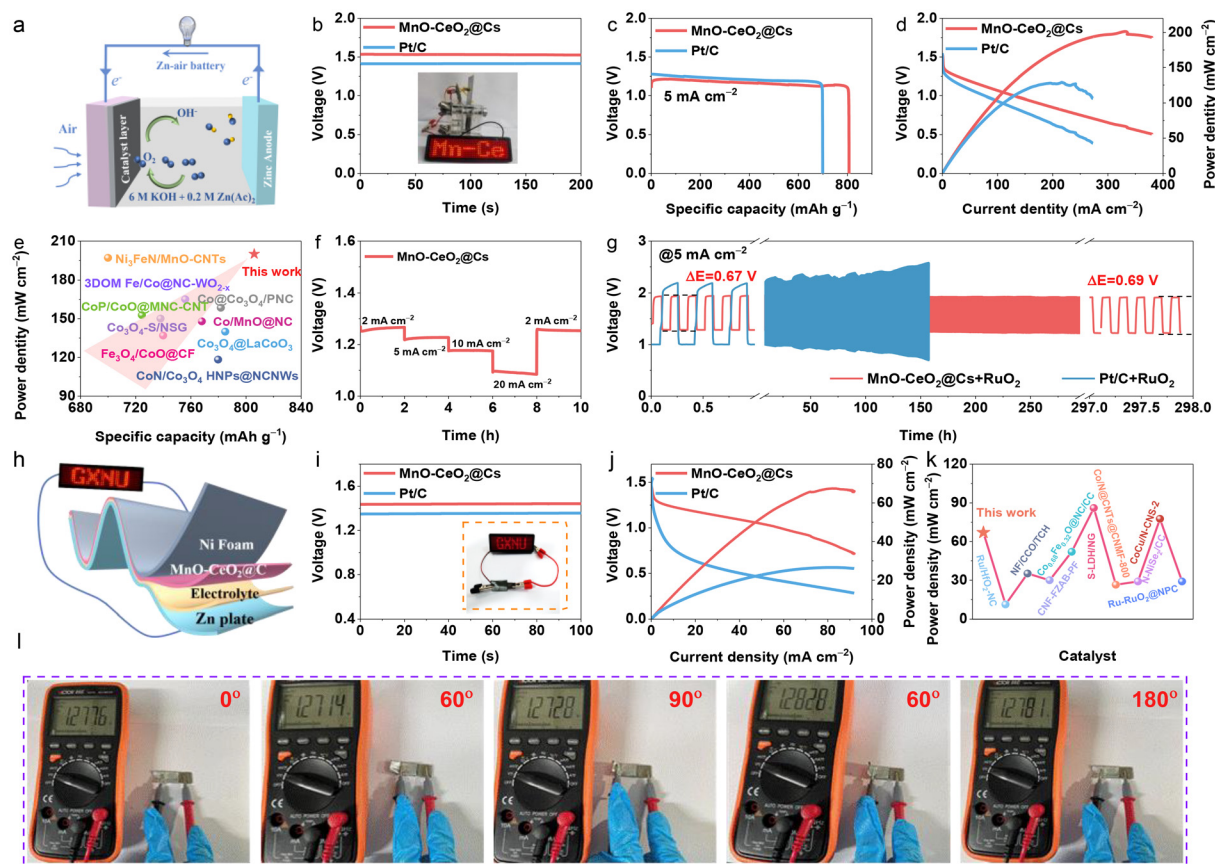


Fig. 5 (a) Schematic configuration of assembled ZAB. (b) Open-circuit voltage (OCV) plots (inset: digital image of LED panel lit by an assembled ZAB). (c) Specific capacity plots. (d) Discharge polarization curves and the corresponding power densities of the catalysts. (e) Comparison of MnO-CeO₂@Cs as air cathode with other recently reported oxide ORR catalysts, in terms of power density and specific capacity. (f) Discharge profiles at various current densities. (g) Galvanostatic cycling at 5 mA cm⁻² (20 min for each cycle). (h) Schematic diagram of the flexible ZAB. (i) OCV of MnO-CeO₂@Cs and Pt/C based flexible ZAB with (inset) LED lighting demonstration of MnO-CeO₂@Cs based flexible ZAB. (j) The discharge polarization and corresponding power density profiles of MnO-CeO₂@Cs and Pt/C based flexible ZAB. (k) Comparison of MnO-CeO₂@Cs as flexible ZAB with other recently reported catalysts. (l) OCV at different bending angles of MnO-CeO₂@Cs based flexible ZAB.

Subsequent electrostatic discharge tests underscored its exceptional rate performance comparable to Pt/C, showing minimal voltage drop during varied current densities (Fig. 5f and Fig. S19†). The long-term stability test is vital for practical applications, the MnO-CeO₂@Cs exhibited a negligible voltage gap decay of only 0.02 V after continuous operation for 297 h, while the Pt/C, CeO₂@Cs, and MnO@Cs alternative began faltering much sooner (Fig. 5g and Fig. S18c†). In light of these impressive aqueous ZAB results, a flexible solid-state ZAB was devised, incorporating carbon cloth laden with MnO-CeO₂@Cs as the cathode, zinc foil anode, and a polyvinyl alcohol (PVA) hydrogel electrolyte (Fig. 5h). The solid-state battery exhibited admirable performance, achieving an OCV of 1.45 V, surpassing Pt/C and other comparable flexible batteries (Fig. 5i and Fig. S20a†). Simultaneously, the flexible ZAB illuminated a red “GXNU” LED panel, emphasizing its practicality (inset of Fig. 5i). The MnO-CeO₂@Cs-based flexible ZAB exhibits an impressive peak power density of 67.4 mW cm⁻², overshadowing the Pt/C variant and most contemporary alternatives (Fig. 5j, k and Fig. S20b, Table S4†). Furthermore, the

MnO-CeO₂@Cs-based flexible ZAB maintained consistent voltage across varying bending angles (0, 90, 180°), reinforcing its adaptability and robustness in flexible configurations (Fig. 5l). The primary factor contributing to the performance improvement is the generation of an optimally oriented BEF by MnO-CeO₂@Cs, which promotes ion/electron migration, thereby accelerating the reaction kinetics at the air cathode.⁵³ Consequently, the MnO-CeO₂@Cs-based ZAB exhibits improved power density and greater cycling stability. Overall, these assessments distinctly highlight the great potential of MnO-CeO₂@Cs for practical energy storage application (from conventional ZAB to flexible battery configurations).

3.4. DFT calculation

To better understand the impact of BEF on the interfacial electronic structure and d-band center (ϵ_d), we performed density functional theory (DFT) calculations, shedding light on the heightened ORR activity of MnO-CeO₂. According to HRTEM results, the MnO (111) and CeO₂ (111) planes were selected as optimized structural models (Fig. S21†). The MnO-CeO₂

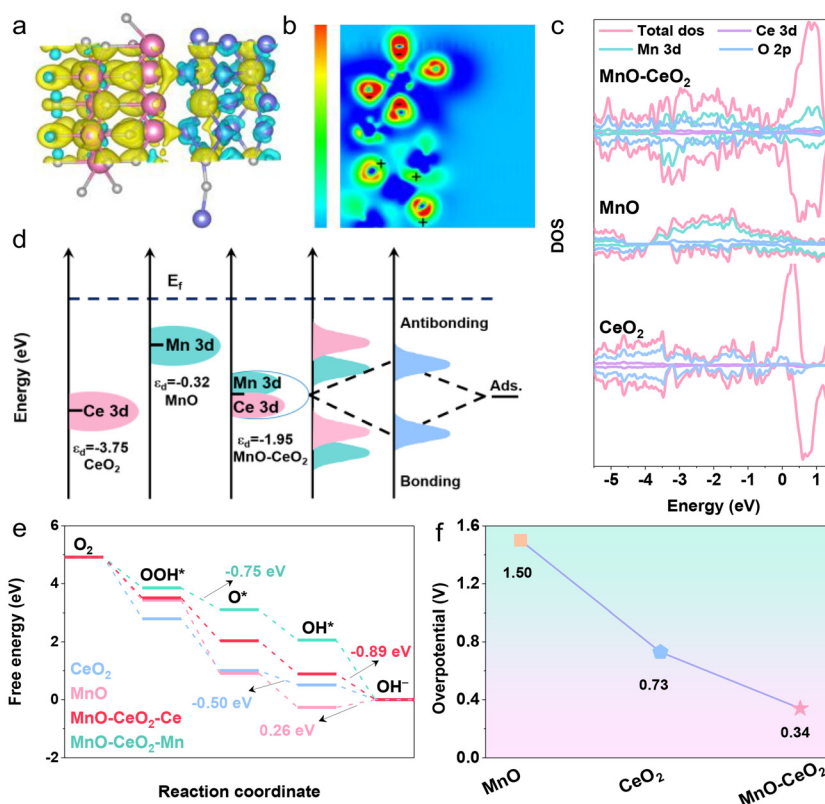


Fig. 6 (a) Differential charge density of MnO-CeO₂. (b) Charge density distribution of MnO-CeO₂, where + and – represent gained and lost electrons, respectively. (c) DOS calculations of MnO, CeO₂ and MnO-CeO₂. (d) Corresponding schematic illustration of bond formation between the reaction surface and the adsorbate (Ads.) and d-band center. (e) Free energy diagrams of MnO, CeO₂ and MnO-CeO₂ towards ORR. (f) Corresponding overpotential for MnO, CeO₂ and MnO-CeO₂.

charge density variation highlights electron transfer dynamics, with regions colored in yellow and cyan indicating electron accumulation and depletion, respectively (Fig. 6a). Evidently, electron loss is pronounced around MnO while being markedly concentrated around CeO₂'s periphery (Fig. 6b). This observation suggests that the coupling of CeO₂ triggers localized charge redistribution at the interface, bolstering electron mobility from MnO to CeO₂, a notion supported by XPS and UPS results. Based on the density of states (DOS) results depicted in Fig. 6c, it is observed that neither electrocatalyst presents a band gap at the Fermi level. Notably, MnO-CeO₂ manifests a heightened DOS adjacent to the Fermi level, indicating its enhanced conductivity and electrocatalytic prowess compared to its MnO and CeO₂ counterparts.⁵⁴ Remarkably, the ϵ_d values for MnO and CeO₂ were -0.32 eV and -3.75 eV, respectively (Fig. 6d), implying that the adsorption of reaction intermediates at these respective sites may be either excessively weak or overly intense. In stark contrast, the ϵ_d of MnO-CeO₂ is -1.95 eV, signifying a balanced adsorption strength. The results suggested that amalgamating CeO₂ with MnO effectively modulated the adsorption strength of ORR intermediates, thereby accelerating the ORR kinetics.²⁷ Notably, the DOS of MnO-CeO₂ in proximity to the E_f predominantly arises from the Mn 3d orbitals, underscoring that MnO plays a pivotal role

in amplifying the overall catalytic conductivity within the reaction matrix.⁵⁵ The Gibbs free energy diagrams for the ORR process were calculated for four configurations (MnO, CeO₂, Mn site in MnO-CeO₂, and Ce site in MnO-CeO₂), as shown in Fig. 6e. The limiting potential (U) is defined by the minimum free energy change in the rate-determining step (RDS) during the ORR process.³⁹ At zero electrode potential, all models consistently present a downward trajectory in their free energy pathway, signifying a near-instantaneous exothermic reaction. The only exception is MnO in the transformation from OH* to OH⁻, which is also the rate-determining step (RDS) in its ORR process. The calculated barrier for the RDS in MnO-CeO₂ (Mn) (OOH + e⁻ → O + OH⁻) is -0.75 V, exceeding the barrier on MnO-CeO₂ (Ce) ($\eta = -0.89$ V). This indicates that MnO-CeO₂ (Ce) has a lower RDS barrier compared to MnO-CeO₂ (Mn), and even lower than MnO (0.26 V) and CeO₂ (-0.50 V). This suggests that the coupling of CeO₂ is crucial for enhancing the ORR activity of MnO, thereby underscoring the likelihood of Ce serving as the active site. Encouragingly, the calculated overpotential (η) of MnO-CeO₂ is 0.34 V, which is more positive than that of MnO ($\eta = 1.50$ V) and CeO₂ ($\eta = 0.73$ V) (Fig. 6f). Collectively, the above results suggest that the formation of the BEF between MnO and CeO₂ led to the interfacial electron redistribution, which effectively fosters optimized adsorption

of oxygen intermediates, ultimately leading to the superior ORR activity of MnO-CeO₂.⁵⁶

4. Conclusions

In summary, we successfully synthesized an oxygen-deficient spherical MnO-CeO₂@Cs electrocatalyst using a high-temperature pyrolysis strategy. The MnO-CeO₂@Cs catalyst exhibits satisfactory ORR activity ($E_{1/2} = 0.80$ V, $j_L = 5.5$ mA cm⁻²) in alkaline conditions. Additionally, the ZAB assembled with MnO-CeO₂@Cs showcases an elevated peak power density of 202.7 mW cm⁻², and displays remarkable stability over 297 h. Experimental results and theoretical calculations unequivocally validate a unique interfacial electronic structure driven by the harmonious synergy between MnO and CeO₂. This distinctive BEF at the MnO-CeO₂@Cs interface fosters a conducive environment for charge redistribution, optimizing the adsorption energy of oxygen intermediates and amplifying the ORR kinetics. Specifically, MnO plays a critical role, particularly through its 3d orbitals, significantly enhancing the overall electrical conductivity and reaction efficiency of the catalyst. This work not only signifies a monumental stride in electrocatalyst development but also paves the way for a novel paradigm in designing interfacial BEFs. This is anticipated to provide a nuanced control over charge distribution on catalyst surfaces, heralding a new era in electrocatalyst design and applications.

Author contributions

Lixia Wang: investigation, conceptualization, writing-original draft. Xinran Hu: investigation. Huatong Li: data curation. Zhiyang Huang: methodology. Jia Huang: data curation. Tayirjan Taylor Isimjan: writing-review & editing. Xiulin Yang: supervision, writing-review & editing.

Conflicts of interest

There are no conflicts to declare.

Acknowledgements

This work is financially supported by the National Natural Science Foundation of China (no. 21965005, 52363028), Natural Science Foundation of Guangxi Province (2021GXNSFAA076001), Guangxi Technology Base and Talent Subject (GUIKE AD18126001, GUIKE AD20297039).

References

- 1 F. Liu and Z. Fan, *Chem. Soc. Rev.*, 2023, **52**, 1723–1772.
- 2 G. Chen, R. Lu, C. Li, J. Yu, X. Li, L. Ni, Q. Zhang, G. Zhu, S. Liu, J. Zhang, U. I. Kramm, Y. Zhao, G. Wu, J. Xie and X. Feng, *Adv. Mater.*, 2023, **35**, 2300907.
- 3 Y. Li, Y. Ding, B. Zhang, Y. Huang, H. Qi, P. Das, L. Zhang, X. Wang, Z.-S. Wu and X. Bao, *Energy Environ. Sci.*, 2023, **16**, 2629–2636.
- 4 L. Peng, L. Shang, T. Zhang and G. I. N. Waterhouse, *Adv. Energy Mater.*, 2020, **10**, 2003018.
- 5 F. Guo, M. Zhang, S. Yi, X. Li, R. Xin, M. Yang, B. Liu, H. Chen, H. Li and Y. Liu, *Nano Res. Energy*, 2022, **1**, 9120027.
- 6 G. Zhang, X. Liu, X. Zhang, Z. Liang, G. Xing, B. Cai, D. Shen, L. Wang and H. Fu, *Chin. J. Catal.*, 2023, **49**, 141–151.
- 7 Q. Wang, L. Shang, R. Shi, X. Zhang, Y. Zhao, G. I. N. Waterhouse, L.-Z. Wu, C.-H. Tung and T. Zhang, *Adv. Energy Mater.*, 2017, **7**, 1700467.
- 8 L. Wang, Y. Qin, H. Li, Z. Huang, M. Gao, T. T. Isimjan and X. Yang, *J. Colloid Interface Sci.*, 2023, **650**, 719–727.
- 9 L. Zong, P. Li, F. Lu, C. Wang, K. Fan, Z. Li and L. Wang, *Adv. Funct. Mater.*, 2023, **33**, 2301013.
- 10 X. F. Lu, Y. Chen, S. Wang, S. Gao and X. W. Lou, *Adv. Mater.*, 2019, **31**, 1902339.
- 11 F. Zhang, R. Ji, X. Zhu, H. Li, Y. Wang, J. Wang, F. Wang and H. Lan, *Small*, 2023, **19**, 2301640.
- 12 Q. Dong, H. Wang, J. Ren, X. Wang and R. Wang, *Chem. Eng. J.*, 2022, **442**, 136128.
- 13 X. Guo, Y. Yuan, S. Li, J. Wang, Z. Bai and L. Yang, *Int. J. Hydrogen Energy*, 2023, **69**, 26805–26816.
- 14 X. Cheng, X. Jiang, S. Yin, L. Ji, Y. Yan, G. Li, R. Huang, C. Wang, H. Liao, Y. Jiang and S. Sun, *Angew. Chem., Int. Ed.*, 2023, **62**, e202306166.
- 15 S. Guo, J. Wang, Y. Sun, L. Peng and C. Li, *Chem. Eng. J.*, 2023, **452**, 139317.
- 16 J. Lee, C. Choi, J. B. Park, S. Yu, J. Ha, H. Lee, G. Jang, Y. S. Park, J. Yun, H. Im, S. Moon, S. Lee, J.-I. Choi, D.-W. Kim and J. Moon, *J. Energy Chem.*, 2023, **83**, 496–508.
- 17 L. Zhai, X. She, L. Zhuang, Y. Li, R. Ding, X. Guo, Y. Zhang, Y. Zhu, K. Xu, H. J. Fan and S. P. Lau, *Angew. Chem., Int. Ed.*, 2022, **61**, e202116057.
- 18 D. Chen, R. Lu, R. Yu, Y. Dai, H. Zhao, D. Wu, P. Wang, J. Zhu, Z. Pu, L. Chen, J. Yu and S. Mu, *Angew. Chem., Int. Ed.*, 2022, **61**, e202208642.
- 19 X. Zhao, M. Liu, Y. Wang, Y. Xiong, P. Yang, J. Qin, X. Xiong and Y. Lei, *ACS Nano*, 2022, **16**, 19959–19979.
- 20 Y. Yang, Y. Huang, S. Zhou, Y. Liu, L. Shi, T. T. Isimjan and X. Yang, *J. Energy Chem.*, 2022, **72**, 395–404.
- 21 Y. Shi, Z.-R. Ma, Y.-Y. Xiao, Y.-C. Yin, W.-M. Huang, Z.-C. Huang, Y.-Z. Zheng, F.-Y. Mu, R. Huang, G.-Y. Shi, Y.-Y. Sun, X.-H. Xia and W. Chen, *Nat. Commun.*, 2021, **12**, 3021.
- 22 C. Hou, Y. Hou, Y. Fan, Y. Zhai, Y. Wang, Z. Sun, R. Fan, F. Dang and J. Wang, *J. Mater. Chem. A*, 2018, **6**, 6967–6976.
- 23 Y. Tian, X. Liu, L. Xu, D. Yuan, Y. Dou, J. Qiu, H. Li, J. Ma, Y. Wang, D. Su and S. Zhang, *Adv. Funct. Mater.*, 2021, **31**, 2101239.

- 24 J. Li, C. Shu, C. Liu, X. Chen, A. Hu and J. Long, *Small*, 2020, **16**, 2001812.
- 25 J. Gao, G. Wang, W. Wang, L. Yu, B. Peng, A. El-Harairy, J. Li and G. Zhang, *ACS Nano*, 2022, **16**, 6255–6265.
- 26 G. Huo, X.-W. Wang, Z.-B. Zhang, Z. Song, X.-M. Kang, M.-X. Chen, Q. Wang, X.-Z. Fu and J.-L. Luo, *J. Energy Chem.*, 2020, **51**, 81–89.
- 27 L. Wang, J. Huang, Z. Huang, H. Li, T. T. Isimjan and X. Yang, *Chem. Eng. J.*, 2023, **472**, 144924.
- 28 X. Xie, L. Shang, R. Shi, G. I. N. Waterhouse, J. Zhao and T. Zhang, *Nanoscale*, 2020, **12**, 13129–13136.
- 29 S.-Y. Lin, L.-X. Xia, L. Zhang, J.-J. Feng, Y. Zhao and A.-J. Wang, *Chem. Eng. J.*, 2021, **424**, 130559.
- 30 Q.-D. Ruan, R. Feng, J.-J. Feng, Y.-J. Gao, L. Zhang and A.-J. Wang, *Small*, 2023, **19**, 2300136.
- 31 J. Xu, J. Wan, W. Zhang, Y. Li, F. Cheng, Z. Cheng, Y. Xu, S. Sun, Q. Li, C. Fang and J. Han, *Adv. Funct. Mater.*, 2023, **33**, 2214613.
- 32 W. Zhong, C. Yang, J. Wu, W. Xu, R. Zhao, H. Xiang, K. Shen, Q. Zhang and X. Li, *Chem. Eng. J.*, 2022, **436**, 134813.
- 33 Y. Liu, Y. Zheng, D. Feng, L. Zhang, L. Zhang, X. Song and Z.-A. Qiao, *Angew. Chem., Int. Ed.*, 2023, **62**, e202306261.
- 34 Q. P. Ngo, T. T. Nguyen, M. Singh, R. Balaji, N. H. Kim and J. H. Lee, *Appl. Catal., B*, 2023, **331**, 122674.
- 35 C. Lyu, J. Cheng, Y. Yang, J. Wu, K. Wu, Y. Yang, W.-M. Lau, N. Wang, D. Pang and J. Zheng, *J. Mater. Chem. A*, 2023, **11**, 4319–4333.
- 36 X. Dong, P. Sun, J. Wu, S. Huang, X. Zeng, S. Wang, X. Chen and D. Cao, *Adv. Compos. Hybrid Mater.*, 2023, **6**, 72.
- 37 J. Cheng, C. Lyu, H. Li, J. Wu, Y. Hu, B. Han, K. Wu, M. Hojamberdiev and D. Geng, *Appl. Catal., B*, 2023, **327**, 122470.
- 38 S. Zhang, C. Tan, R. Yan, X. Zou, F.-L. Hu, Y. Mi, C. Yan and S. Zhao, *Angew. Chem., Int. Ed.*, 2023, **62**, e202302795.
- 39 S. Zhang, Y. Wang, X. Wei, L. Chu, W. Tian, H. Wang and M. Huang, *Appl. Catal., B*, 2023, **336**, 122926.
- 40 H. Li, C. Chen, Y. Yan, T. Yan, C. Cheng, D. Sun and L. Zhang, *Adv. Mater.*, 2021, **33**, 2105067.
- 41 L. Wang, Z. Huang, H. Huang, S. Zhong, M. Huang, T. T. Isimjan and X. Yang, *Electrochim. Acta*, 2022, **404**, 139598.
- 42 Q. Zhou, S. Hou, Y. Cheng, R. Sun, W. Shen, R. Tian, J. Yang, H. Pang, L. Xu, K. Huang and Y. Tang, *Appl. Catal., B*, 2021, **295**, 120281.
- 43 J. Luo, X. Wang, Y. Gu, S. Wang, Y. Li, T. Wang, Y. Liu, Y. Zhou and J. Zhang, *Chem. Eng. J.*, 2023, **472**, 144839.
- 44 D. Liu, J. Tian, Y. Tang, J. Li, S. A. Wu, S. Yi, X. Huang, D. Sun and H. Wang, *Chem. Eng. J.*, 2021, **406**, 126772.
- 45 B. Guo, X. Niu, J. Yang, L. Li, Q. Chen and J. Zhou, *Chem. Eng. J.*, 2023, **472**, 145126.
- 46 L. Wang, H. Yu, Z. Huang, Z. Luo, T. T. Isimja, S. Xu and X. Yang, *Electrochim. Acta*, 2023, **443**, 141932.
- 47 J. Cai, H. Zhang, L. Zhang, Y. Xiong, T. Ouyang and Z.-Q. Liu, *Adv. Mater.*, 2023, **35**, 2303488.
- 48 X. Zhao, J. Chen, Z. Bi, S. Chen, L. Feng, X. Zhou, H. Zhang, Y. Zhou, T. Wågberg and G. Hu, *Adv. Sci.*, 2023, **10**, 2205889.
- 49 J. Rong, E. Gao, N. Liu, W. Chen, X. Rong, Y. Zhang, X. Zheng, H. Ao, S. Xue, B. Huang, Z. Li, F. Qiu and Y. Qian, *Energy Storage Mater.*, 2023, **56**, 165–173.
- 50 L. Wang, M. Huang, M. Gao, T. T. Isimjan and X. Yang, *Mater. Chem. Front.*, 2023, **7**, 2628–2636.
- 51 C. Hu, Q. Liang, Y. Yang, Q. Peng, Z. Luo, J. Dong, T. T. Isimjan and X. Yang, *J. Colloid Interface Sci.*, 2023, **633**, 500–510.
- 52 M. Guo, M. Xu, Y. Qu, C. Hu, P. Yan, T. T. Isimjan and X. Yang, *Appl. Catal., B*, 2021, **297**, 120415.
- 53 G. Fu, J. Wang, Y. Chen, Y. Liu, Y. Tang, J. B. Goodenough and J.-M. Lee, *Adv. Energy Mater.*, 2018, **8**, 1802263.
- 54 J. Niu, C. Geng, X. Liu and A. P. O'Mullane, *Chem. Eng. J.*, 2023, **468**, 143607.
- 55 W.-D. Zhang, Q.-T. Hu, L.-L. Wang, J. Gao, H.-Y. Zhu, X. Yan and Z.-G. Gu, *Appl. Catal., B*, 2021, **286**, 119906.
- 56 J. Qin, H. Liu, P. Zou, R. Zhang, C. Wang and H. L. Xin, *J. Am. Chem. Soc.*, 2022, **144**, 2197–2207.